PAPER

Check for updates

Reduction of NO$_x$ on metal-free hydrogenated hexagonal boron nitride†

Anthony J. R. Payne, iD * Neubi F. Xavier Jr iD and Marco Sacchi iD *

Sustainable catalysts are essential for critical industrial and environmental processes. 2D materials have exceptional surface area and unique thermal and electronic properties, making them excellent candidates for catalytic applications. Moreover, 2D materials can be functionalised to create metal-free active sites, which provide sustainable alternatives to transition and precious metals. Among the pollutants emitted by combustion engines, NO$_x$ stands out as one of the most detrimental gases, contributing to environmental pollution and posing risks to human health. We demonstrate that functionalised defects in hexagonal boron nitride (hBN) provide a thermodynamically viable route to removing NO$_x$ by reaction with a hydrogenated boron vacancy (3HV$_B$). The decomposition of NO$_2$ proceeds by initially overcoming an activation energy barrier of 1.12 eV to transfer a hydrogen atom from the surface, forming a NO$_2$H species, followed by the elimination of a water molecule. A thermodynamically favourable product consisting of a surface-bound hydroxyl adjacent to a nitrogen antisite defect (where a nitrogen atom occupies a site typically occupied by a boron atom) forms after overcoming an energy barrier of 1.28 eV. NO can further decompose by overcoming an activation energy barrier of 2.23 eV to form a surface HNO species. A rearrangement of the HNO species takes place with an activation energy of 1.96 eV, followed by the elimination of water. The overall reactions reduce NO$_x$ into defective hBN and H$_2$O.

1 Introduction

The high temperatures and pressures experienced during fuel combustion enable the fixation of N$_2$ and O$_2$, resulting in NO and NO$_2$ emissions (referred to as NO$_x$).[1] NO$_x$ is known to cause ailments such as impaired lung function and irritation of the eyes and throat.[2,3] The environment is adversely affected by NO$_x$ dissolving in rainwater, forming nitric acid (HNO$_3$), and creating acid rain.[4] Acid rain has many detrimental effects, including hindering plant growth above and below ground and damaging plant leaves, with food-producing plants most severely affected.[5,6] NO$_x$ pollution can contaminate soils and water bodies, leading to eutrophication and acidification.[7] Furthermore, NO$_2$ is the starting point for the photochemical formation of ground-level ozone,[8,9] leading to further detrimental effects on ecosystems and thousands of premature deaths.[10–12] The World Health Organisation Global Air Quality Guidelines specify a NO$_2$ limit of 10 g m^{-3} as an annual average; however, this limit is often exceeded in major cities such as New York, London, Paris, Delhi and Beijing.[13]

The main emitters of NO$_x$ are vehicles (with diesel engines being exceptionally high emitters),[14] power plants, agricultural and industrial processes.[15,16] Despite technological advances in engine manufacturing and the rapid increase of electric vehicles, fossil fuels still make up a large proportion of the energy market to meet demand.[17] Hence, much research has focused on eliminating the toxic and polluting gases emitted by fossil fuel combustion.[18]

Using metal-based heterogeneous catalysts for emission control is widely accepted as an effective way of reducing pollution from NO$_x$ and gas exhaust emissions, with many vehicles equipped with selective catalytic reduction (SCR) systems.[19,20] SCR reduces NO$_x$ into environmentally benign N$_2$ and H$_2$O by utilising a catalyst and reducing agent.[21] Reducing agents include NH$_3$ and H$_2$ in NH$_3$-SCR and H$_2$-SCR. NH$_3$-SCR has shown to be an attractive choice for low-temperature reduction; however, challenges include N$_2$O formation and the need for an additional system to supply and store ammonia in applications.[21,22] Safe storage and distribution of H$_2$ remain technological challenges which delay the widespread employment of hydrogen use as a fuel.[23] However, recently, there has been significant interest in producing H$_2$ "on-demand" *via* water-gas shift reaction post-combustion (CO + H$_2$O → CO$_2$ + H$_2$),[24] thus providing a source of H$_2$ for H$_2$-SCR. Presently, automotive catalysts dominate the global demand for platinum group metals,[25]

School of Chemistry and Chemical Engineering, University of Surrey, Guildford, GU2 7XH, UK. E-mail: apayne@surrey.ac.uk, m.sacchi@surrey.ac.uk

† Electronic supplementary information (ESI) available. See DOI: https://doi.org/10.1039/d4cy00206g

4264 | *Catal. Sci. Technol.*, 2024, **14**, 4264–4273

This journal is © The Royal Society of Chemistry 2024

with platinum and palladium commonly employed for H_2-SCR.[21] However, platinum and palladium catalysts often exhibit peak activity at temperatures around 200 °C,[21] whereas catalytic converters in vehicles frequently surpass this threshold with passenger vehicles operating over a wide range of temperatures (280–650 °C).[26] Therefore, there is potential to find alternative catalysts that are active at higher temperatures. Perovskites have recently been of interest as a greener alternative for NO_x removal but still rely (although quantitatively less) on metal atoms in their structure.[27,28] Metal-free NH_3-SCR has been investigated using ketone-terminated graphene nanoribbon edges,[29,30] yet metal-free H_2-SCR remains underexplored within a critically significant field.

Hexagonal boron nitride (hBN) consists of sp^2 hybridised boron and nitrogen atoms forming single-atom thick nanosheets.[31] These so-called '2D' nanosheets are held together by van der Waals forces and stacked in an ABAB pattern.[32] Due to the B–N bond's ionic character, charge localisation[33] hBN is an insulator with a large band gap of 6 eV. Potential applications of hBN include electrical,[34] optoelectronic[35] and spintronic[36] devices. Due to its outstanding antiwear and antifriction properties, hBN is also employed in the automotive industry as a lubricant.[37] hBN can be grown by various methods. Bottom-up approaches include chemical vapour deposition (CVD), which uses boron and nitrogen-containing precursors, such as borazine or ammonia borane, to grow epitaxial, single layers of hBN on a metal substrate.[38] Alternatively, hBN can be formed by reacting molecules containing boron and nitrogen, such as boric oxide and urea.[39] In each case, a single layer of hBN can be produced by subsequent physical or chemical exfoliation.[40]

hBN has high thermal stability,[31,41] a low coefficient of thermal expansion,[42] and a high specific surface area;[43] these properties make hBN ideally suited for industrial catalysis. Through high-resolution transmission electron microscopy, hBN has been found to contain various vacancy defects, including boron (V_B) and nitrogen (V_N) single-atom vacancies.[44,45] Ball milling has been established as an effective method for creating additional defect sites on hBN.[46,47] Using V_N as an active site to remove NO_2 has already been the subject of previous density functional theory (DFT) studies.[48,49] In these earlier studies, the V_N defect was repaired, and molecular oxygen was produced. Pd and Ni-doped hBN have also been considered to catalyse NO reduction by CO to form N_2 and CO_2.[50] Other dopants such as carbon,[51] silicon,[52] and rhodium[53] doped hBN have also been investigated for the fabrication of sensors for NO_2.

Research on hBN defects has shown the hydrogenated V_B (HV_B) to be significantly more stable than the hydrogenated V_N defect and the non-hydrogenated counterpart V_B supported by X-ray absorption and luminescence measurements.[54,55] We have previously reported that HV_B vacancies can be effectively produced by exposing boron–nitrogen divacancies to ammonia.[56] Furthermore, as hydrogen atoms are ordinarily contained in hBN precursors, HV_B defects are likely to be generated during hBN processing, such as during the growth of hBN nanowalls.[57]

Previous work by Nash et al.[58] investigated HV_B defects as active sites for the hydrogenation of alkenes on metal-free hBN. The authors reported a reactor based on a pebble mill to introduce HV_B defects by mechanical force. The hydrogenation reaction was achieved with high yields of 97–100% for several alkenes. The work was supported by DFT calculations, which determined a barrier for the hydrogenation of propane to propane of 1.53 eV. Given the activity of HV_B defects in the hydrogenation of alkenes, other similar reactions may be possible.

A deep understanding of the molecular level mechanisms is required to develop more efficient and greener NO_x catalysts. This study investigates the reactivity of the HV_B with NO and NO_2 molecules. Our computational study shows that HV_B defects in hBN can provide an excellent metal-free site for removing NO_x by providing a stable source of hydrogen for reduction.

2 Computational methodology

First-principles electronic structure calculations were carried out using CASTEP.[59] The PBE functional[60] was used to treat exchange and correlation in combination with the Tkatchenko–Scheffler dispersion correction method.[61] The plane wave basis set was expanded to a cut-off energy of 400 eV. All calculations used Vanderbilt ultrasoft pseudopotentials[62] and a Monkhorst–Pack k-point sampling of the first Brillouin zone[63] with a uniform grid of $(10 \times 10 \times 1)$ or $(4 \times 4 \times 1)$ for modelling of (1×1) and (5×5) unit cells, respectively. The surface structures were optimised until the maximum force on each atom was less than 0.025 eV Å^{-1} and a self-consistent field energy tolerance of 1×10^{-6} eV. During relaxation, the lattice parameters remained fixed to those of a pristine hBN unit cell. The transition states along the reaction pathways were identified with the linear and quadratic synchronous transit (LST/QST) algorithm,[64] with a force tolerance of 0.1 eV Å^{-1}. A (5×5) unit cell was employed for all defect calculations, with a vacuum region of at least 20 Å to separate the periodically repeated images and avoid spurious interactions. Molecular diagrams were produced using VESTA.[65]

Adsorption energies E_{Ads} were calculated using the standard formula:

$$E_{Ads} = E_{AB} - E_A - E_B \tag{1}$$

where E_{AB} is the energy of the adsorbed species, E_A and E_B are the energy of the dissociated species.

Formation energies E_f were calculated using the formula:

$$E_f = E_V - E_{hBN} + \frac{1}{2} n_N E_{N_2} + n_B E_B - \frac{1}{2} n_H E_{H_2} \tag{2}$$

where E_V is the energy of a vacancy or system, E_{hBN} is the energy of the pristine hBN sheet, n_N and n_B are the number of nitrogen and boron atoms removed to create a vacancy, respectively. E_{N_2} is the energy of an isolated N_2 molecule, E_B

is the reference energy of a boron atom in its α-rhombohedral phase,[66] n_H is the number of hydrogen atoms added to hydrogenated vacancies and E_{H_2} is the energy of an isolated H_2 molecule.

Reaction rate coefficients (K_{TST}) for the surface reactions were calculated according to the transition state theory:

$$k_{TST} = \frac{k_b T}{h} \frac{q^\ddagger}{q} \exp\left(-\frac{\Delta E_a}{k_b T}\right) \quad (3)$$

where k_b is the Boltzmann constant, T is the temperature, h is the Plank constant, $q^\ddagger$ and q are the partition functions for the transition state and initial state, respectively, and ΔE_a is the activation energy. The adsorption rate coefficients k_{ads} were calculated using Hertz–Knudsen kinetics:[67]

$$k_{ads} = \frac{PA}{\sqrt{2\pi m k_b T}} \quad (4)$$

where P is the partial pressure of the molecule, A is the surface area of the surface site, m is the mass of the particle k_b is the Boltzmann constant and T is the temperature.
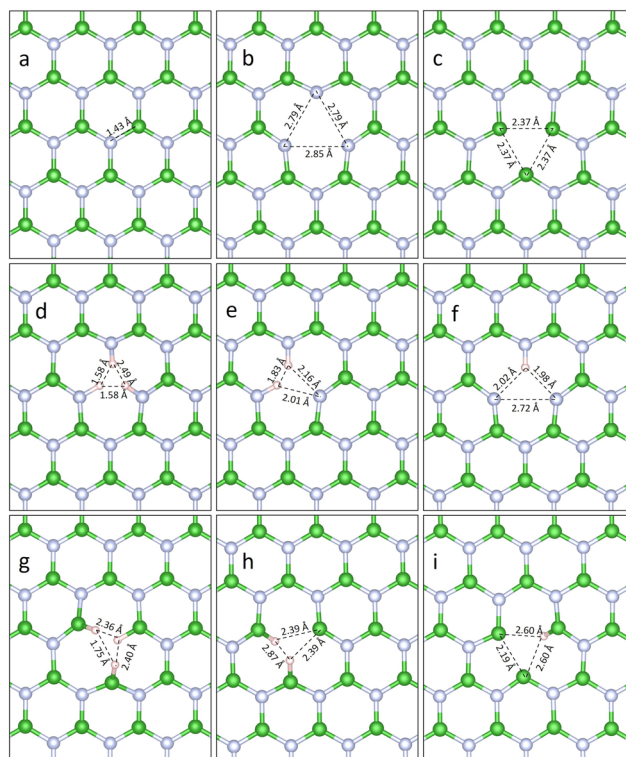
3 Results and discussion

Each of the vacancy models can be seen in Fig. 1. The structure and properties of V_B and V_N vacancies have been

Fig. 1 (a) Pristine hBN sheet, (b) V_B (E_f = 9.75 eV, spin = 1 μ_B) (c) V_N (E_f = 8.63 eV, spin = 1 μ_B), (d) $3HV_B$ (E_f = 1.98 eV, spin = 0 μ_B), (e) $2HV_B$ (E_f = 4.22 eV, spin = 1 μ_B), (f) $1HV_B$ (E_f = 6.82 eV, spin = 0 μ_B), (g) $3HV_N$ (E_f = 5.29 eV, spin = 0 μ_B), (h) $2HV_N$ (E_f = 6.86 eV, spin = 1 μ_B), (i) $1HV_N$ (E_f = 6.93 eV, spin = 0 μ_B). Boron atoms are shown in green, and nitrogen atoms are shown in grey.

discussed in detail in previous work and are shown in b and c.[56] V_N is more stable than V_B with E_f of 8.63 eV and 9.75 eV, respectively. V_B has C_{2v} symmetry, whereas V_N has D_{3h} symmetry due to Jahn–Teller distortion.[68–71] Fig. 1d shows an HV_B with all three nitrogen dangling bonds saturated by hydrogen atoms ($3HV_B$); it is by far the most stable configuration investigated, with a low E_f of 1.98 eV. The geometry of $3HV_B$ can be rationalised through a combination of electronic and steric factors. Comparing the N–H–N angle (θ) variation between vacancies, we can rationalise the increase in in-plane steric hindrance as a function of the increasing number of adsorbed hydrogens. In $3HV_B$, only one of the three hydrogen atoms points into the hBN plane with a θ of 180° and Hirshfeld charge of +0.07 e. The remaining two hydrogens point above and below the hBN plane where θ is 130° with a Hirshfeld charge of +0.11 e. This difference in angle can be explained by the need to prevent steric clashes of hydrogen atoms and minimise partial positive charges yet maintain sp^2 hybridisation of the hBN as much as possible. The H–H distance is 2.49 Å between the outer hydrogens and 1.58 Å between the in-plane hydrogen and each external hydrogen, with an average H–H distance of 1.88 Å. The in-plane nitrogen has a 0.08 e higher N–H bond population than the average N–H bond, reflecting a greater extent of sp^2 hybridisation and stronger bonding. The minor change in bond population results in the N–H in-plane bond being shorter by 0.008 Å (0.8%) than the out-of-plane N–H bonds. This minor change in bond length is unlikely to affect the reactivity of $3HV_B$ significantly.

Removing a hydrogen atom to create a $2HV_B$ increases E_f to 4.22 eV. In $2HV_B$, the hydrogen atoms are further coplanar with hBN, with an average θ of 155°, and have an H–H distance of 1.83 Å. The loss of a hydrogen atom allows the remaining hydrogens to be orientated more in the plane as there is now less steric hindrance inside the vacancy, allowing for θ values closer to 180°. In $2HV_B$, the N–H distances are 2.01 Å and 2.16 Å; therefore, one hydrogen atom is slightly closer to the nitrogen atom in this structure. The hydrogens interact with the lone pair on the nitrogen dangling bond asymmetrically, thus reducing the N–H distance for the interacting H. $2HV_B$ has a magnetic moment of 1 μ_B due to an unpaired electron on the nitrogen dangling bond. These changes in the geometry of $2HV_B$ are not enough to compensate for creating a dangling bond, decreasing the stability of this defect relative to that of $3HV_B$.

The $1HV_B$ has a higher E_f of 6.82 eV due to the creation of an additional nitrogen-dangling bond. Here, only one hydrogen atom remains on the vacancy; the reduced steric clashes allow for an θ of 157°. It follows that the remaining hydrogen is positioned only slightly above the hBN plane with H–N distances of 1.98 Å and 2.02 Å. Removal of the final hydrogen will form a V_B with an E_f of 9.75 eV. It is clear that the stability of HV_B increases with an increasing number of hydrogen atoms; hence, $3HV_B$ is the most likely to form and will be the subject of our investigation for the hydrogenation of NO_2.

4266 | *Catal. Sci. Technol.*, 2024, **14**, 4264–4273

This journal is © The Royal Society of Chemistry 2024

In addition to $1-3HV_B$, we also investigated the structure and geometry of hydrogenated V_N vacancies ($1-3HV_N$) for comparison and are shown in Fig. 1(g–i). The configurations obtained by DFT are in good agreement with the work presented in Surya *et al.*[72] with a detailed comparison provided in the ESI.† Of these vacancies, $3HV_N$ has the lowest E_f of 5.29 eV, significantly higher than that of $3HV_B$ (E_f 1.98 eV). The greater decrease in formation energy of boron vacancies compared to nitrogen vacancies upon the addition of hydrogen atoms can be rationalised by considering the electronegativity and geometry of the atoms around the vacancy. As N is more electronegative than B, the N–H bonding is stronger than that of B–H, with average bond lengths of 1.10 Å and 1.19 Å for $3HV_B$ and $3HV_N$. Furthermore, longer B–H bonds lead to an increased steric clash of hydrogen atoms, requiring greater deformation of the vacancy site. Therefore, $3HV_B$ vacancies maintain stronger N–B bonding than $3HV_N$ with average B–N bond lengths of H-connected atoms of 1.42 Å and 1.44 Å, respectively. Given the stability observed in the $3HV_B$ vacancy and the likelihood of the formation of hydrogenated V_B vacancies compared to hydrogenated V_N, we have elected to focus our investigation primarily on this site.
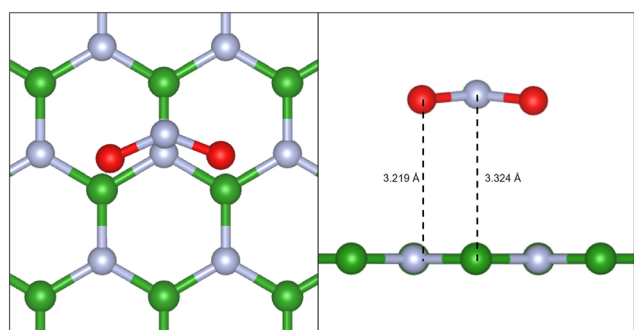
3.1 NO$_2$ decomposition

The adsorption of NO$_2$ on pristine hBN was initially considered. A range of sites and orientations were investigated (as described in the ESI†), with the most stable adsorption site pictured in Fig. 2. Here, NO$_2$ is adsorbed with the nitrogen atom at a height of 3.32 Å above hBN with the O–N–O plane almost parallel to the hBN plane. In this position, NO$_2$ has an E_{Ads} of −0.202 eV, indicative of physisorption. Previous works have also investigated the adsorption of NO$_2$ on hBN and have found the orientation with oxygen atoms pointing upwards, away from the surface, to be the preferred orientation,[52] with one study providing an E_{Ads} of −0.09 eV.[49] However, these studies used generalised gradient approximation exchange–correlation functionals without dispersion corrections, thus underestimating dispersion forces

Fig. 2 Adsorption site and orientation of NO$_2$ on hBN. The oxygen atoms are angled slightly towards the hBN plane at a height of 3.219 Å. The nitrogen is situated at a height of 3.324 Å. This adsorption position maximises attractive dispersion forces between hBN and NO$_2$ with an E_{Ads} of −0.202 eV.

and the adsorption energy of physisorption. In our study, initiating geometry optimisation with the oxygen atoms pointing away from the surface leads to a rotation of the NO$_2$ molecule, resulting in a parallel orientation. The particular stability of NO$_2$ parallel to the plane can be rationalised by considering that the dispersion interaction between the hBN and NO$_2$ is maximised by increasing the contact area between the adsorbate and the substrate. The boron atoms of hBN and NO$_2$ oxygen atoms have average Hirshfeld charges of 0.21 e and −0.07 e, respectively; these charges attract stabilising the adsorbed NO$_2$.

The step-wise mechanism for the reaction of NO$_2$ with $3HV_B$ was then considered by exploring multiple possible reaction pathways to ensure the minimum energy path was found (as described in the ESI†). The reaction mechanism, starting from the adsorption of NO$_2$ above $3HV_B$ and ending with the creation of a nitrogen antisite defect (N_B) and H$_2$O, can be seen in Fig. 3 with the overall equation NO$_2$ + $3HV_B$ ⇌ N_B + H$_2$O + OH. This reaction pathway, TS1–9, consists of nine elementary steps that connect reactants, intermediates, and products through transition states. Fig. S5 of the ESI† displays each structure along the reaction path from both perpendicular and parallel orientations. The highest transition state barrier in TS1–9 is 1.28 eV (TS7), and the ΔE of the reaction is −0.99 eV, indicating that this reaction is possible at moderate temperatures and is thermodynamically favourable. We will examine each of these steps in turn.
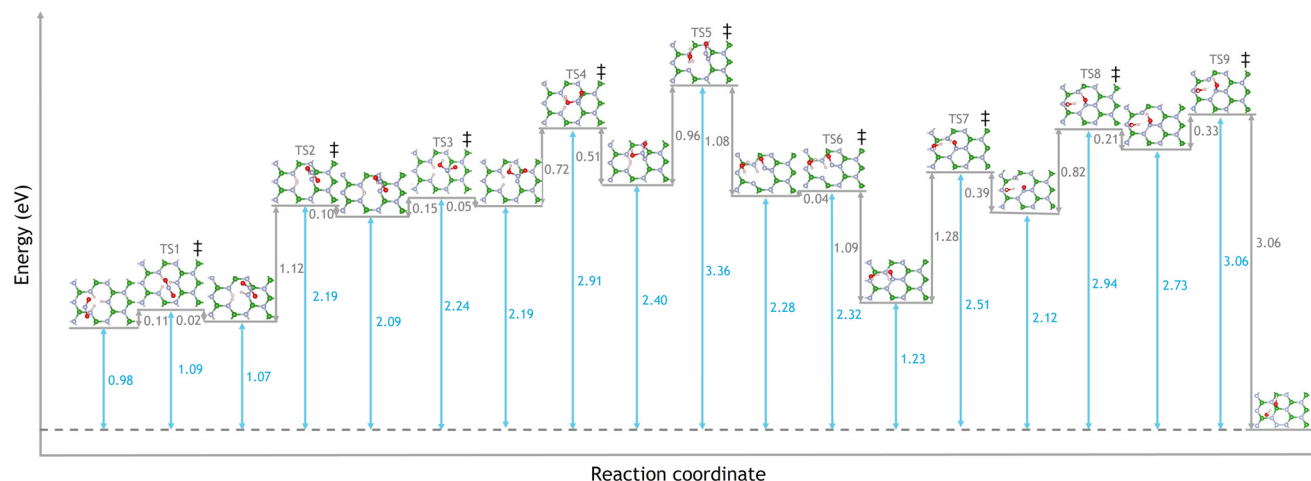
Firstly, a range of NO$_2$ adsorption sites on $3HV_B$ and orientations were examined (Fig. S2 of the ESI†). The adsorption energy minimum can be seen in Fig. 4a with an E_{Ads} of −0.247 eV, compared to −0.202 eV for physisorption on pristine hBN. Here, NO$_2$ is oriented to bring one of the oxygen atoms close to the surface at a height of 2.93 Å (Fig. 4a). Hydrogen bonding between the oxygen lone pair and the hydrogen pointing above the hBN plane stabilises this orientation with an O–H distance of 2.28 Å, reducing its adsorption energy relative to pristine hBN. Prior to the reaction, the adsorbed NO$_2$ diffuses to a position where an oxygen atom is directly above a hydrogen atom of $3HV_B$ after overcoming a low energy barrier of 0.11 eV (TS1).

Next, hydrogen transfer from $3HV_B$ to NO$_2$ was considered to create a NO$_2$H species in a NO$_2$ + $3HV_B$ ⇌ NO$_2$H reaction step. A range of orientations was assessed to find the most stable NO$_2$H conformation. The most stable position of NO$_2$H is close to the vacancy, with an O–H bond directly above the nitrogen dangling bond and with the second oxygen atom above a surface boron atom. Structural relaxations of other geometries either resulted in the formation of $3HV_B$ or produced a higher energy NO$_2$H orientation. As with NO$_2$ adsorption on pristine hBN, the NO$_2$H is stabilised by van der Waals interactions between the oxygen lone pair and surface boron (Fig. 4b). The N–H bond-breaking step requires an activation energy of 1.02 eV (TS2). The products of this step are a $2HV_B$ and a NO$_2$H species. Hydrogen bonding between the NO$_2$H hydrogen moiety and the uncoordinated surface nitrogen gives NO$_2$H an E_{Ads} of −0.28 eV.

This journal is © The Royal Society of Chemistry 2024

Catal. Sci. Technol., 2024, **14**, 4264–4273 | **4267**

Fig. 3 The reaction pathway of NO_2 with a $3HV_B$ to N_B and H_2O. The product of the reaction, a nitrogen antisite adjacent to a boron site with a hydroxyl group, is used as the reference energy. Transition states are identified by ‡ and labelled TS1–9. The highest energy barrier, TS7, reflects the movement of a hydrogen atom through the hBN plane in preparation for making an N_B site. Other steps occur with energy barriers between 0.04 and 1.09 eV. The reaction is thermodynamically favourable with a ΔE of −0.99 eV.
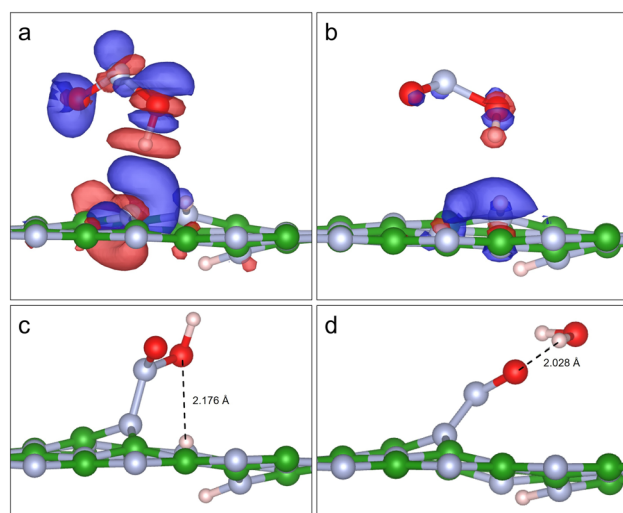
The NO_2H species can easily rotate parallel to the hBN plane. The NO_2H rotation proceeds *via* an initial step with a low activation barrier of only 0.15 eV to bring the oxygen atoms parallel to the plane (TS3), as shown in Fig. 5b. This barrier reflects the breaking of van der Waals forces between the surface and NO_2H. A second rotation occurs with a more significant energy barrier of 0.72 eV (TS4). This higher barrier reflects the need to overcome the repulsive forces of the nitrogen lone pairs and form an N–N bond between NO_2H and the surface nitrogen dangling bond. NO_2H is now chemisorbed onto the surface, as shown in Fig. 5c. Here, the surface nitrogen is puckered 0.5 Å above the plane, and the N–N bonded nitrogen atoms have sp^3 hybridised character. Subsequently, after forming a NO_2H species, the hydroxyl can accept another hydrogen atom to produce water (TS5, NO_2H + H ⇌ NO + H_2O) after overcoming an energy barrier of 0.96 eV. The produced water molecule is hydrogen bonded to the

surface. Adsorbed water could remain on the surface and contribute to stabilising further structures and transition states through hydrogen bonding; therefore, it continues to feature in our simulations.

Following the formation of a water molecule (TS5), the surface structure now contains an O═N–N moiety, a nitrogen dangling bond in the vacancy, and an N–H group. Bonding of the O═N nitrogen to the nitrogen dangling bond can
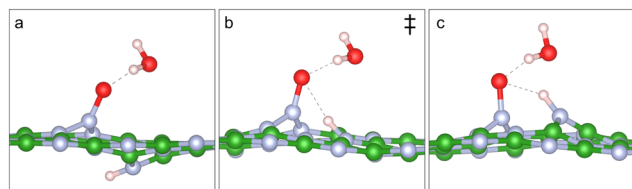

Fig. 5 (a) Adsorption site of NO_2H over $2HV_B$ with an E_{Ads} of −0.38 eV. (b) NO_2H adsorbed over $2HV_B$ before reaction to form a chemisorbed NO_2H species (c). The rotation barrier from (a) to (b) is 0.15 eV. The transition from (b) to (c) has a barrier of 0.72 eV. Charge accumulation is shown in blue, and charge depletion in red with respect to an isolated NO_2H (isosurface cut-off in (a) and (b) is 0.01 e Å^{-3}). (a) Shows a much greater change in charge densities due to the stronger van der Waals interactions with the surface. NO_2H decomposes to produce H_2O after overcoming a reaction barrier of 0.96 eV to change from (c) to (d).

Fig. 4 (a) Adsorption geometry of NO_2 over a $3HV_B$ with an E_{Ads} of −0.25 eV. (b) NO_2 adsorbed over a $3HV_B$ prior to reaction with an E_{Ads} of −0.16 eV. NO_2 can migrate from (a) to (b) by overcoming a low energy barrier of 0.11 eV. (c) NO_2H adsorbed over $2HV_B$ with an E_{Ads} of −0.38 eV. The barrier to transferring a hydrogen atom from (b) to (c) is 1.12 eV.

4268 | *Catal. Sci. Technol.*, 2024, **14**, 4264–4273

This journal is © The Royal Society of Chemistry 2024

Fig. 6 (a) N_B with additional oxygen and hydrogen atoms positioned above and below the hBN plane, respectively (b) transition state to bring the hydrogen atom from below to an above plane position with a barrier of 1.28 eV (TS7). (c) N_B with additional oxygen and hydrogen atoms both positioned above the plane.

substantially lower the total energy of the surface. This step occurs after overcoming a low barrier of 0.04 eV (TS6) and forms a nitrogen antisite defect (N_B), where the nitrogen atom occupies the site usually occupied by boron in hBN. The N_B nitrogen atom is bound to both the nitrogen atoms of the vacancy and the oxygen atom above, as seen in Fig. 6a. Further surface rearrangement takes place to bring the sub-layer hydrogen through the vacancy before positioning itself above the plane 1.87 Å away from the surface oxygen. This rearrangement occurs with an energy barrier of 1.28 eV (TS7) due to steric hindrance destabilising the transition state as the hydrogen needs to pass through an in-plane position (Fig. 6b), and the subsequent geometry has moved the N–O bond into a sp^3-like orientation. These steric factors cause TS7 to proceed with the highest barrier in the decomposition of NO_2.

Surface hydrogen and oxygen atoms can now form a surface hydroxyl group bound to the antisite nitrogen (N_B) after overcoming an energy barrier of 0.82 eV, as shown in TS8, reflecting the breaking of an N–H bond and the forming of an H–O bond ($RN-H + N_BO \rightleftharpoons RN + N_BO-H$). Given the electron density accumulation provided by the four nitrogen atoms and the oxygen around the N_B, it is thermodynamically favourable for the hydroxyl species to migrate to an adjacent boron atom as it has a lower electron density, as shown in Fig. 7. The migration through TS9 (with an energy barrier of 0.33 eV) minimises the electron repulsion and satisfies the remaining nitrogen dangling bond, reducing the overall energy of the product.

The overall reaction forms a water molecule and a surface-bound hydroxyl adjacent to a nitrogen antisite defect ($NO_2 + 3HV_B \rightleftharpoons N_B + H_2O + OH$). This reaction is thermodynamically favourable to form with a ΔE of −0.98 eV. The highest energy barrier for a single step in the overall NO_2 reduction mechanism is 1.28 eV. The barrier for the reaction of NO_2 with HV_B is comparable to that of NO_2 with V_N as explored in work by Feng *et al.*[49] where NO_2 decomposes to form O_2 and the 'healing' of V_N to form a pristine hBN sheet with a barrier of 1.17 eV. We note that this paper did not include dispersion correction in the DFT calculations, therefore likely underestimating the energy of adsorption. Given the low formation energy of the initial $3HV_B$ defect, the relatively low energy barrier of the rate-determining step and the production of a thermodynamically favourable product, the catalytic reduction of NO_2 over hydrogenated hBN defects
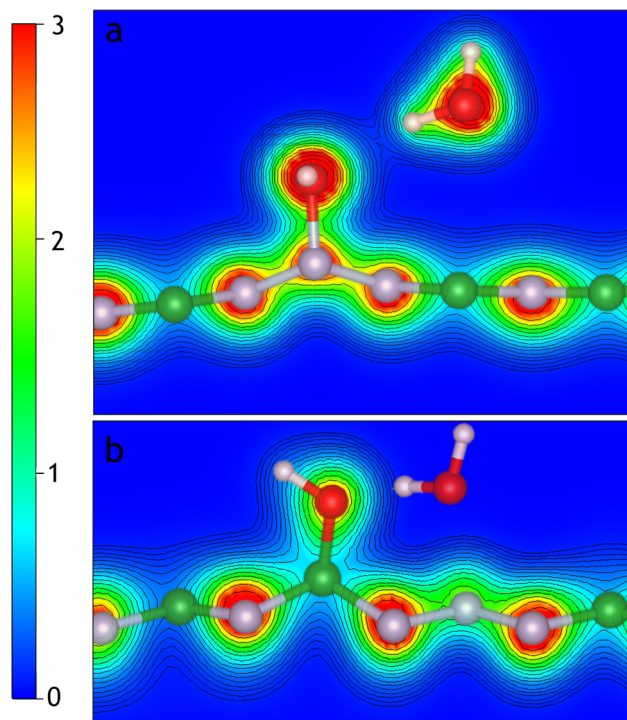
Fig. 7 Electron density slice contour map from 0 to 3 e Å^{-3} of (a) N_B with attached hydroxyl functional group and (b) N_B adjacent to a surface boron site with a hydroxyl group attached. The barrier to transition from (a) to (b) is 0.33 eV (TS9) in an exothermic process with a reaction enthalpy of −2.73 eV. Note: the water molecule is in the plane of the slice in (b) but not in (a). In (b), the electron density surrounding the N_B site repels that of the adsorbed oxygen. Therefore, the hydroxyl migrates to an adjacent boron site (a), lowering electron–electron repulsion and producing a more thermodynamically stable product.

appears to be a promising way of controlling NO_2 emissions from combustion engines.

If an additional hydrogen atom is added, further steps could be taken to produce a second water molecule, as shown in Fig. 8. The hydroxyl group can then be hydrogenated to form a second water molecule ($OH + \frac{1}{2}H_2 \rightleftharpoons H_2O$) after overcoming an energy barrier of 0.36 eV (TS10). This step is exothermic with an overall ΔE of −1.30 eV. The thermodynamic stability is due to the creation of a second water molecule, the return to sp^2 binding of the surface boron atom and the original water molecule being able to adsorb strongly on top of the N_B site. An isolated N_B has an E_f of 5.45 eV, higher than that of a $2HV_B$ vacancy with an E_f of 4.22 eV. The overall product of the reaction $NO_2 + 3HV_B + H \rightleftharpoons N_B + 2H_2O$ between NO_2 and a $3HV_B$, in the presence of hydrogen atoms, is an N_B and two water molecules. Once exhausted, new vacancy defects need to be introduced to regenerate active sites. The difference in E_f between N_B and $3HV_B$ is 3.47 eV, thus requiring an input of energy to regenerate the active site. The introduction of such sites can be achieved by mechanical methods such as ball milling,[46,47] and has been achieved in work by Nash *et al.*[58] to complete a catalytic cycle.

The overall reaction of NO_2 to N_B and two water molecules is thermodynamically feasible, yet many activated steps are
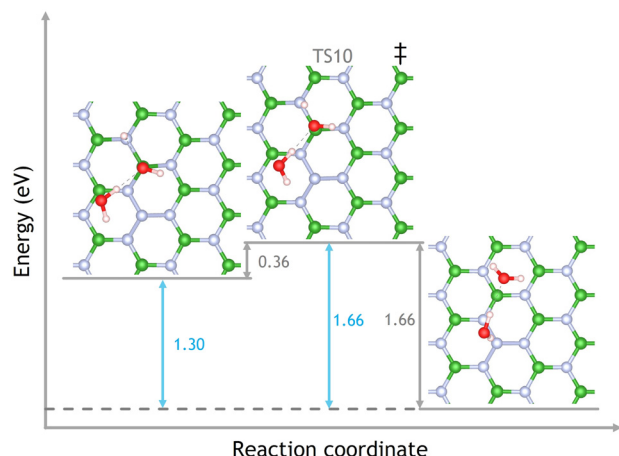
This journal is © The Royal Society of Chemistry 2024

Catal. Sci. Technol., 2024, **14**, 4264–4273 | **4269**

Fig. 8 Reaction step of the hydroxyl group on a surface-born atom adjacent to a N_B site with an adsorbed hydrogen atom. Transition states are identified by ‡ labelled TS10. An energy barrier of 0.36 eV facilitates the hydrogenation of the hydroxyl group to create a water molecule as the product. This step is thermodynamically favourable with a ΔE of −1.30 eV.

involved. Therefore, a microkinetic model consisting of 10 elementary steps was constructed to evaluate the reaction's kinetic viability. The consumption of NO_2 and production of H_2O at different temperatures, and a pressure of 10 bar was chosen to align with the optimal conditions for the water-gas shift reaction[24] (further details of the microkinetic model are reported in the ESI†). The rate of NO_2 consumption compared to the rate of H_2O formation was calculated with results shown in Fig. 9. Below 800 K, the rate of NO_2 consumption remains very low ($<1.10 \times 10^{-6}$ s^{-1}); increasing the temperature, the rate of H_2O production rises to a maximum of 7.48×10^{-5} s^{-1} at 990 K, accompanied by a NO_2 consumption rate of 3.68×10^{-5} s^{-1}. As temperatures rise, the energy of the molecules increases, allowing multiple reaction barriers to be overcome. Beyond the optimal temperature, the reactants cease to adsorb onto the surface and persist in
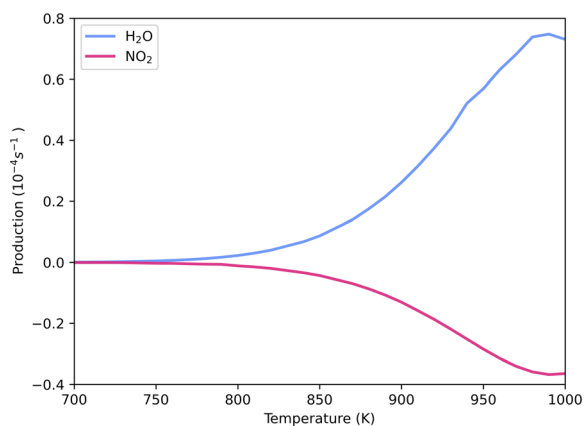
the gas phase. Our results show that NO_2 decomposition can occur at $3HV_B$ defect sites in hBN *via* a Langmuir–Hinshelwood mechanism.

3.2 NO decomposition

NO pollution shares many of the same detrimental effects as NO_2 pollution leading to acid rain; hence, these two species and their effects are often combined in NO_x. Moreover, NO oxidised to NO_2 by reacting with sources of O.[73] We included the reaction of NO in the scope of our work to explore any possible reactions with $3HV_B$. Adsorption of NO was first considered above pristine hBN. The most favourable adsorption site is pictured in Fig. 10 and adsorbs with an E_{Ads} of −0.17 eV, similar to NO_2.

NO adsorption on $3HV_B$ was considered by starting with the most stable orientation pictured in Fig. 11 with an E_{Ads} of −0.240 eV at a height of 3.041 Å, similar to NO_2. Multiple reaction routes were then analysed; here, the reaction begins with the direct reaction of NO with $3HV_B$ to form a chemisorbed HNO species after overcoming a high energy barrier of 2.23 eV (TS11, NO + $3HV_B$ ⇌ HNO + $2HV_B$). The size of this barrier reflects the breaking of the N–H bond and stretching of the N–O bond to accommodate the additional coordination of the nitrogen atom, partially stabilised by the nitrogen lone pair orientated towards the surface hydrogen. This step has the highest barrier for the reaction of NO with $3HV_B$. Hydrogen transfer to produce a hydroxyl group occurs with another high energy barrier of 1.96 eV (TS12). Following the creation of a hydroxyl group, the NOH intermediate can accept an N–H hydrogen atom in TS13 (ΔE of 1.63 eV) to form a chemisorbed HNOH species and a dangling bond over the nitrogen atom. The reaction's final step (TS14) involves the migration of the nitrogen atom to bind with the nitrogen dangling bond of the vacancy to create an N_B site with a remaining hydrogen attached (HN_B). Simultaneously, the hydroxyl group accepts a hydrogen atom to form a water molecule. The overall reaction NO + $3HV_B$ ⇌ H_2O + HN_B is slightly exothermic with a ΔE of −0.09 eV. The surface product of the reaction (HN_B) has an E_f of 5.42 eV.

Fig. 9 Microkinetic simulations for the reaction of NO_2 and $3HV_B$ displaying the consumption of NO_2 compared to the production of H_2O as a function of temperature.
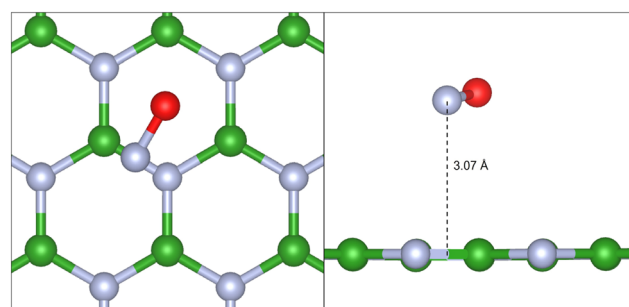

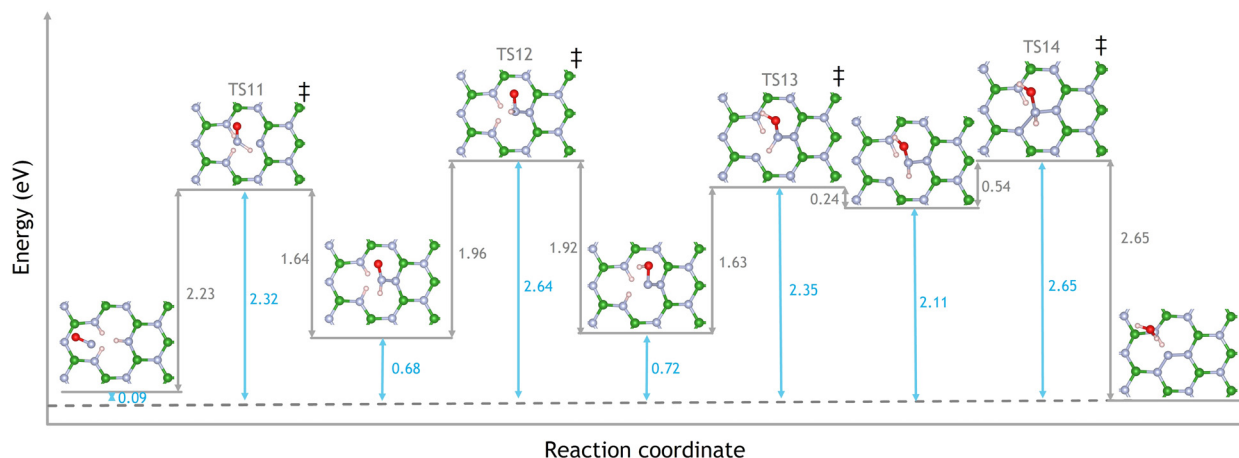**Fig. 10** Adsorption site and orientation of NO on hBN. The nitrogen atom is angled slightly towards the hBN plane at a height of 3.07 Å. The oxygen atom is situated in the centre of a hBN ring. This adsorption position maximises attractive dispersion forces between hBN and NO_2 with an E_{Ads} of −0.17 eV.

4270 | *Catal. Sci. Technol.*, 2024, **14**, 4264–4273

This journal is © The Royal Society of Chemistry 2024

Fig. 11 The reaction pathway of NO with a 3HV$_B$ to N$_B$ and H$_2$O. The product of the reaction, a molecule of water and an N$_B$ site with the final surface hydrogen remaining, is used as a reference energy. Transition states are identified by ‡ and labelled TS11–14. The highest energy barrier at TS1 (2.23 eV) reflects the energy to break an N–H bond and lengthen the N–O bond simultaneously. The reaction is thermodynamically favourable with a ΔE of −0.09 eV.

The reaction pathway of NO with 3HV$_B$ significantly differs from that of NO$_2$. For NO reduction, the hydrogen transfer to create a chemisorbed HNO$_x$ species occurs with a much higher energy barrier than NO$_2$, with activation energies of 2.23 eV and 1.28 eV, respectively, for this step. The weaker N–O bonds in NO$_2$ with O=N–O and O–N=O resonance structures result in greater electron density on the oxygen atoms, making an O=N–O–H species possible. Thus, NO$_2$ can accept a hydrogen atom from 3HV$_B$ to form a physisorbed NO$_2$H species before chemisorption. In contrast, NO has a stronger N–O bond with less electron density available to accept a hydrogen atom on the O or N atoms. Therefore, hydrogen transfers and chemisorption occur in a single step with a higher energy barrier, with O–H and N–N bonds forming simultaneously. The barriers relating to NO decomposition on 3HV$_B$ are significantly higher than those revealed in work by Xiao et al.[48] where the reaction of NO with a V$_N$ results in the formation of a B–O–N epoxy structure. The reaction of 3HV$_B$ with NO is less exothermic with a ΔE of −0.09 compared to NO$_2$ with a ΔE of −0.98 eV. Here, the product of the reaction is an N$_B$ site with an additional N–H bond pointing hydrogen below the hBN monolayer.

Our results show that NO$_2$ decomposition is energetically facile at 3HV$_B$ defect sites in hBN with a barrier of 1.28 eV and achieves optimum NO$_2$ consumption at 990 K. The decomposition product is H$_2$O, an N$_B$ site adjacent to a surface hydroxyl species. This hydroxyl species can then be hydrogenated to yield a second water molecule. Similarly, NO can be decomposed by NO with a limiting step of 2.23 eV to create an N$_B$ and a vacancy hydrogen.

calculations. NO$_2$ decomposition proceeds via Langmuir–Hinshelwood hydrogenation of NO$_2$ to form a NO$_2$H species before the chemisorption of this intermediate on the hBN vacancy. The reaction follows several further steps that end with eliminating a molecule of water, forming an N$_B$ site adjacent to a surface-bound hydroxyl. An additional hydrogen atom diffusing from other sites can react with the hydroxyl and yield a second water molecule. The atomistic details of the NO$_2$ reduction mechanism, encompassing ten elementary steps, have been described in section 3, focusing on linking reaction energy and barriers to steric and electronic effects. Our calculations prove that the decomposition of NO$_2$ over hydrogenated hBN vacancies is a feasible approach to removing NO$_2$. The rate-determining step has an energy barrier of 1.28 eV. Using micro-kinetics to evaluate the reaction path as a whole, we have calculated an optimum temperature of 990 K under a pressure of 10 bar with a very low rate of reaction below 800 K. The NO decomposition proceeds via the formation of a surface HNO species before rearrangement and elimination of a water molecule before forming an N$_B$. The NO reaction mechanism progresses through four steps (discussed in section 3.2). The decomposition of NO to N$_B$ + H$_2$ has an energy barrier of 2.32 eV and is slightly exothermic (0.09 eV). Therefore, higher temperatures are required to achieve NO reduction. These reactions transform harmful and polluting NO$_2$ into benign H$_2$O using a selective and metal-free catalyst. This paper has thoroughly investigated the complete removal of NO$_x$ 3HV$_B$ defects in hBN, demonstrating its potential to be developed as an effective metal-free catalyst for deNO$_x$ applications.

4 Conclusions

In conclusion, we have investigated the reaction of NO$_x$ with a 3HV$_B$ site in a "free-standing" hBN mono-layer using DFT

Data availability

The datasets generated and/or analysed during the current study are available in the University of Surry research repository: **https://doi.org/10.15126/surreydata.901080**.

Author contributions

Conflicts of interest

There are no conflicts to declare.

Acknowledgements

References

1 A. A. Abdel-Rahman, *Int. J. Energy Res.*, 1998, **22**, 483–513.
2 M. Kampa and E. Castanas, *Environ. Pollut.*, 2008, **151**, 362–367.
3 M. Guarnieri and J. R. Balmes, *Lancet*, 2014, **383**, 1581–1592.
4 A. Singh and M. Agrawal, *J. Environ. Biol.*, 2008, **29**, 15–24.
5 Z. Shi, J. Zhang, Z. Xiao, T. Lu, X. Ren and H. Wei, *J. Environ. Manage.*, 2021, **297**, 113213.
6 E. Du, D. Dong, X. Zeng, Z. Sun, X. Jiang and W. de Vries, *Sci. Total Environ.*, 2017, **605–606**, 764–769.
7 W. de Vries, *Curr. Opin. Environ. Sci. Health*, 2021, **21**, 100249.
8 L. F. Gamon and U. Wille, *Acc. Chem. Res.*, 2016, **49**, 2136–2145.
9 P. Sicard, E. Paoletti, E. Agathokleous, V. Araminienė, C. Proietti, F. Coulibaly and A. De Marco, *Environ. Res.*, 2020, **191**, 110193.
10 E. Agathokleous, Z. Feng, E. Oksanen, P. Sicard, Q. Wang, C. J. Saitanis, V. Araminiene, J. D. Blande, F. Hayes, V. Calatayud, M. Domingos, S. D. Veresoglou, J. Peñuelas, D. A. Wardle, A. de Marco, Z. Li, H. Harmens, X. Yuan, M. Vitale and E. Paoletti, *Sci. Adv.*, 2020, **6**, 1–18.
11 D. Nuvolone, D. Petri and F. Voller, *Environ. Sci. Pollut. Res.*, 2018, **25**, 8074–8088.
12 P. Sicard, Y. O. Khaniabadi, S. Perez, M. Gualtieri and A. De Marco, *Environ. Sci. Pollut. Res.*, 2019, **26**, 32645–32665.
13 A. Goshua, C. A. Akdis and K. C. Nadeau, *Allergy*, 2022, **77**, 1955–1960.
14 R. O'Driscoll, M. E. Stettler, N. Molden, T. Oxley and H. M. ApSimon, *Sci. Total Environ.*, 2018, **621**, 282–290.
15 A. T. Hoang, T. T. Huynh, X. P. Nguyen, T. K. T. Nguyen and T. H. Le, *Energy Sources, Part A*, 2021, **00**, 1–21.
16 D. H. Nguyen, C. Lin, C. T. Vu, N. K. Cheruiyot, M. K. Nguyen, T. H. Le, W. Lukkhasorn, T. D. H. Vo and X. T. Bui, *Environ. Technol. Innovation*, 2022, **28**, 102809.
17 T. Ahmad and D. Zhang, *Energy Rep.*, 2020, **6**, 1973–1991.
18 A. G. Olabi, D. Maizak and T. Wilberforce, *Sci. Total Environ.*, 2020, **748**, 141249.
19 S. Dey and N. S. Mehta, *Resour. Environ. Sustain.*, 2020, **2**, 100006.
20 T. Selleri, A. D. Melas, A. Joshi, D. Manara, A. Perujo and R. Suarez-Bertoa, *Catalysts*, 2021, **11**, 404.
21 S. Muhammad Farhan, W. Pan, C. Zhijian and Y. JianJun, *Fuel*, 2024, **355**, 129364.
22 W. Shan and H. Song, *Catal. Sci. Technol.*, 2015, **5**, 4280–4288.
23 H. Nazir, N. Muthuswamy, C. Louis, S. Jose, J. Prakash, M. E. Buan, C. Flox, S. Chavan, X. Shi, P. Kauranen, T. Kallio, G. Maia, K. Tammeveski, N. Lymperopoulos, E. Carcadea, E. Veziroglu, A. Iranzo and A. M. Kannan, *Int. J. Hydrogen Energy*, 2020, **45**, 20693–20708.
24 W. H. Chen and C. Y. Chen, *Appl. Energy*, 2020, **258**, 114078.
25 A. E. Hughes, N. Haque, S. A. Northey and S. Giddey, *Resources*, 2021, **10**, 93.
26 A. H. Laskar, M. Y. Soesanto and M. C. Liang, *Environ. Sci. Technol.*, 2021, **55**, 4378–4388.
27 S. Royer, D. Duprez, F. Can, X. Courtois, C. Batiot-Dupeyrat, S. Laassiri and H. Alamdari, *Chem. Rev.*, 2014, **114**, 10292–10368.
28 I. V. Yentekakis, A. G. Georgiadis, C. Drosou, N. D. Charisiou and M. A. Goula, *Nanomaterials*, 2022, **12**, 1042.
29 J. Yuan, J. X. Mi, R. Yin, T. Yan, H. Liu, X. Chen, J. Liu, W. Si, Y. Peng, J. Chen and J. Li, *ACS Catal.*, 2022, **12**, 1024–1030.
30 J. Yuan, Z. Wang, J. Liu, J. Li and J. Chen, *Environ. Sci. Technol.*, 2023, **57**, 606–614.
31 S. N. Perevislov, *Refract. Ind. Ceram.*, 2019, **60**, 291–295.
32 C. R. Hsing, C. Cheng, J. P. Chou, C. M. Chang and C. M. Wei, *New J. Phys.*, 2014, **16**, 113015.
33 G. Cassabois, P. Valvin and B. Gil, *Phys. Rev. B*, 2016, **93**, 1–6.
34 S. A. Tawfik, S. Ali, M. Fronzi, M. Kianinia, T. T. Tran, C. Stampfl, I. Aharonovich, M. Toth and M. J. Ford, *Nanoscale*, 2017, **9**, 13575–13582.
35 X. Lü, S. He, H. Lian, S. Lv, Y. Shen, W. Dong and Q. Duan, *Appl. Surf. Sci.*, 2020, **531**, 147262.
36 F. Zheng, G. Zhou, Z. Liu, J. Wu, W. Duan, B. L. Gu and S. B. Zhang, *Phys. Rev. B: Condens. Matter Mater. Phys.*, 2008, **78**, 1–5.
37 P. M. Revabhai, R. K. Singhal, H. Basu and S. K. Kailasa, *J. Nanostruct. Chem.*, 2023, **13**, 1–41.
38 M. Jana and R. N. Singh, *Int. Mater. Rev.*, 2018, **63**, 162–203.
39 R. T. Paine and C. K. Narulat, *Chem. Rev.*, 1990, **90**, 73–91.
40 T. H. Le, Y. Oh, H. Kim and H. Yoon, *Chem. – Eur. J.*, 2020, **26**, 6360–6401.
41 D. R. Lide, G. Baysinger, L. I. Berger, R. N. Goldberg, H. V. Kehiaian, K. Kuchitsu, G. Rosenblatt, D. L. Roth and D.

4272 | *Catal. Sci. Technol.*, 2024, **14**, 4264–4273

This journal is © The Royal Society of Chemistry 2024

Zwillinger, *CRC Handbook of Chemistry and Physics, Internet Version 2005*, CRC Press, Boca Raton, FL, 2005.

42 Q. Cai, D. Scullion, W. Gan, A. Falin, S. Zhang, K. Watanabe, T. Taniguchi, Y. Chen, E. J. Santos and L. H. Li, *Sci. Adv.*, 2019, **5**, eaav0129.

43 L. Xue, B. Lu, Z. S. Wu, C. Ge, P. Wang, R. Zhang and X. D. Zhang, *Chem. Eng. J.*, 2014, **243**, 494–499.

44 C. Jin, F. Lin, K. Suenaga and S. Iijima, *Phys. Rev. Lett.*, 2009, **102**, 1–4.

45 J. C. Meyer, A. Chuvilin, G. Algara-Siller, J. Biskupek and U. Kaiser, *Nano Lett.*, 2009, **9**, 2683–2689.

46 Y. Ding, F. Torres-Davila, A. Khater, D. Nash, R. Blair and L. Tetard, *MRS Commun.*, 2018, **8**, 1236–1243.

47 L. H. Lu, Y. Chen, B. Gavin, Z. Hongzhou, P. Mladen and M. G. Alexey, *J. Mater. Chem. C*, 2011, **21**, 11862–11866.

48 B. Xiao, X. F. Yu and Y. H. Ding, *RSC Adv.*, 2014, **4**, 22688–22696.

49 J. W. Feng, Y. J. Liu and J. X. Zhao, *J. Mol. Model.*, 2014, **20**, 2307.

50 M. D. Esrafili, S. Heydari and L. Dinparast, *Struct. Chem.*, 2019, **30**, 1647–1657.

51 M. D. Esrafili and F. Arjomandi Rad, *Vacuum*, 2019, **166**, 127–134.

52 Y. He, D. Li, W. Gao, H. Yin, F. Chen and Y. Sun, *Nanoscale*, 2019, **11**, 21909–21916.

53 J. Zhang, J. Tian, Q. Zhang, Y. Lu, L. Li and Y. Xu, *ChemistrySelect*, 2021, **6**, 13609–13615.

54 N. L. McDougall, J. G. Partridge, R. J. Nicholls, S. P. Russo and D. G. McCulloch, *Phys. Rev. B*, 2017, **96**, 144106.

55 L. Weston, D. Wickramaratne, M. Mackoit, A. Alkauskas and C. G. Van De Walle, *Phys. Rev. B*, 2018, **97**, 214104.

56 A. J. R. Payne, N. F. Xavier, G. Bauerfeldt and M. Sacchi, *Phys. Chem. Chem. Phys.*, 2022, **24**, 20426–20436.

57 D. Q. Hoang, P. Pobedinskas, S. S. Nicley, S. Turner, S. D. Janssens, M. K. Van Bael, J. D'Haen and K. Haenen, *Cryst. Growth Des.*, 2016, **16**, 3699–3708.

58 D. J. Nash, D. T. Restrepo, N. S. Parra, K. E. Giesler, R. A. Penabade, M. Aminpour, D. Le, Z. Li, O. K. Farha, J. K. Harper, T. S. Rahman and R. G. Blair, *ACS Omega*, 2016, **1**, 1343–1354.

59 M. K. Agusta and I. Prasetiyo, *J. Phys.: Condens. Matter*, 2002, **14**, 2717–2744.

60 J. P. Perdew, K. Burke and M. Ernzerhof, *Phys. Rev. Lett.*, 1996, **77**, 3865–3868.

61 A. Tkatchenko and M. Scheffler, *Phys. Rev. Lett.*, 2009, **102**, 6–9.

62 D. Vanderbilt, *Phys. Rev. B: Condens. Matter Mater. Phys.*, 1990, **41**, 7892.

63 H. J. Monkhorst and J. D. Pack, *Phys. Rev. B: Solid State*, 1976, **13**, 5188.

64 T. A. Halgren and W. N. Lipscomb, *Chem. Phys. Lett.*, 1977, **49**, 225–232.

65 K. Momma and F. Izumi, *J. Appl. Crystallogr.*, 2011, **44**, 1272–1276.

66 K. Shirai, H. Dekura, Y. Mori, Y. Fujii, H. Hyodo and K. Kimura, *J. Phys. Soc. Jpn.*, 2011, **80**, 084601.

67 I. Filot, *Introduction to microkinetic modeling*, Technische Universiteit Eindhoven, 2018.

68 M. S. Si and D. S. Xue, *Phys. Rev. B: Condens. Matter Mater. Phys.*, 2007, **75**, 1–4.

69 B. Huang and H. Lee, *Phys. Rev. B: Condens. Matter Mater. Phys.*, 2012, **86**, 1–8.

70 J. Strand, L. Larcher and A. L. Shluger, *J. Phys.: Condens. Matter*, 2020, **32**, 055706.

71 K. Watanabe and T. Taniguchi, *Phys. Rev. B: Condens. Matter Mater. Phys.*, 2009, **79**, 1–4.

72 V. Surya, K. Choutipalli, K. Esackraj and E. Varathan, *Appl. Surf. Sci.*, 2022, **602**, 15.

73 J. H. Seinfeld and S. N. Pandis, *Atmospheric Chemistry and Physics: From air pollution to climate change*, John Wiley & Sons, 3rd edn, 2016.

This journal is © The Royal Society of Chemistry 2024

Catal. Sci. Technol., 2024, **14**, 4264–4273 | **4273**